IOP Publishing J. Phys. Mater. 6 (2023) 015001 https://doi.org/10.1088/2515-7639/aca82f

Journal of Physics: Materials

OPEN ACCESS

RECEIVED
14 October 2022

REVISED
28 November 2022

ACCEPTED FOR PUBLICATION
1 December 2022

PUBLISHED
15 December 2022

PAPER

Charge transport in single polymer fiber transistors in the sub-100 nm regime: temperature dependence and Coulomb blockade

Jakob Lenz[1], **Martin Statz**[2], **K Watanabe**[3], **T Taniguchi**[4], **Frank Ortmann**[5] **and R Thomas Weitz**[1,2,6,*]

[1] AG Physics of Nanosystems, Faculty of Physics, Ludwig-Maximilians-University Munich, Munich, Germany
[2] 1st Institute of Physics, Faculty of Physics, Georg-August-University, Göttingen, Germany
[3] Research Center for Functional Materials, National Institute for Materials Science, 1-1 Namiki, Tsukuba 305-0044, Japan
[4] International Center for Materials Nanoarchitectonics, National Institute for Materials Science, Tsukuba, Japan
[5] School of Natural Sciences, Department of Chemistry, Technical University of Munich, 85748 Garching b. München, Germany
[6] International Center for Advanced Studies of Energy Conversion (ICASEC), University of Göttingen, Göttingen, Germany
* Author to whom any correspondence should be addressed.

E-mail: thomas.weitz@uni-goettingen.de

Keywords: organic semiconductor, organic electronics, charge transport, Coulomb blockade

Supplementary material for this article is available online

Abstract

Even though charge transport in semiconducting polymers is of relevance for a number of potential applications in (opto-)electronic devices, the fundamental mechanism of how charges are transported through organic polymers that are typically characterized by a complex nanostructure is still open. One of the challenges which we address here, is how to gain controllable experimental access to charge transport at the sub-100 nm lengthscale. To this end charge transport in single poly(diketopyrrolopyrrole-terthiophene) fiber transistors, employing two different solid gate dielectrics, a hybrid Al_2O_3/self-assembled monolayer and hexagonal boron nitride, is investigated in the sub-50 nm regime using electron-beam contact patterning. The electrical characteristics exhibit near ideal behavior at room temperature which demonstrates the general feasibility of the nanoscale contacting approach, even though the channels are only a few nanometers in width. At low temperatures, we observe nonlinear behavior in the current–voltage characteristics in the form of Coulomb diamonds which can be explained by the formation of an array of multiple quantum dots at cryogenic temperatures.

1. Introduction

Organic (semi-)conducting polymers are of significant scientific and technological interest due to their use in organic solar cells, light emitting diodes, batteries, neuromorphic devices, sensors and field-effect transistors. Despite this manifold of existing and potential applications, the fundamental question of how charges are transported through conductive polymers requires further investigation due to the complex structure-property relation between local morphology and charge conduction. A significant problem in this respect has been to locally identify the relative role of the main contributing factors towards the conductivity, namely the inter- and intrachain charge transport. Intrachain transport critically depends on the conjugation length, which in turn depends on the chain rigidity. The interchain mobility on the other hand depends on the π–π overlap of adjacent repeat units, and is enhanced in crystalline regions of polymer assemblies. The relative weights of intra- and interchain transport in turn depend critically on the paracrystallinity of the polymer film that is typically composed of nanoscale crystalline regions connected via amorphous regions, whereas in the latter the so-called tie chains are located [1]. Their importance as conductive highways connecting nanocrystalline regions of the polymers has been highlighted extensively [1–3]. Recently it was also found that additionally, nominally non-conductive parts can support conductivity via providing

tunneling pathways [4]. A summarized overview of charge transport mechanism in polymeric semiconductors at the nanoscale can be found in our recent review [5].

Not only the nanoscale morphology of polymer thin films is complex, but also the interaction between charges travelling through the films and the molecular structure (polaron formation) and the Coulomb interaction between charges itself [6–8]. A viable route to study the structure-performance relationship has been via electrostatically-gated thin-film field-effect transistors, that allow the investigation of charge transport mechanisms as function of polymer morphology and charge carrier density, while charge transport is typically studied at the macroscale with lateral device dimensions well above 1 μm [9]. This has allowed to advance our understanding of charge transport significantly despite the indirect nature of such measurements. To allow for a more direct access to local charge transport, we have developed a contacting scheme that enables accessing the hard-to-probe sub-100 nm local transport regime.

To develop the local probe scheme, we focus on a model organic semiconductor, namely the semiconducting donor–acceptor copolymer poly{2,2′-[(2,5-bis(2-hexyldecyl)-3,6-dioxo-2,3,5,6-tetrahydropyrrolo[3,4-c]pyrrole-1,4-diyl)dithiophene]-5,5′-diyl-alt-thiophen-2,5-diyl} (PDPP, $M_n = 4.1E + 4$ g mol^{-1}) which is known to be a good hole conductor in organic solar cells [10], and has shown excellent performance in thin film transistors [11, 12]. For example, charge-carrier density independent field-effect mobilities of up to 3 cm^2 V^{-1}s^{-1} (with quadratic ($\gamma = 2$ [13]) relation of I_D to V_{GS}–V_{on} at lower temperatures; a clear indication of trap-free charge transport) as well as excellent stability under ambient conditions was demonstrated. Furthermore, PDPP also showed performance when measured in bulk films at the nanoscale in a vertical geometry, in which electrical transport at distances below 10 nm could be realized. There, it was found that if thin nanoscale films are gated by an electrolyte, unexpectedly ultra-high current densities of MA cm^{-2} can be realized [14, 15]. However, this geometry was still relying on nanometer-thin films of the PDPP polymer or on thin films of multiple crystalline fibers. These crystalline fibers are a few nanometers in height and several hundreds of nanometers in length and are composed of agglomerates of individual polymer chains that are aligned along the long axes of the fibers. These fibers can be aligned e.g. by doctor blading into macroscopically aligned films [16]. In such films it was identified by optical spectroscopy and x-ray diffraction measurements that the individual polymer chains are aligned along the long axis of the fibers. [16] The possibility to deposit such polymer fibers provides the exciting perspective to be able to measure charge transport along individual crystallites. However, up to now contacting such individual fibers has not been demonstrated.

2. Results and discussion

To study charge transport at the nanoscale, we employ a field-effect transistor geometry with a solid gate dielectric. This has the advantage with respect to electrolyte gating of allowing to study temperature-dependent charge transport as a function of charge carrier density for both electron and hole transport, thereby allowing to identify different charge transport mechanisms and regimes. In order to still realize well-functioning transistors, special care had to be taken to maintain sufficient gate coupling to remain within the gradual channel approximation. This can be realized by decreasing the gate dielectric thickness and by using high-k gate oxides. We investigate single fiber transistors with channel lengths below 100 nm using two different gate/gate dielectric configurations, schematically depicted in figures 1(a) and (b). First, a hybrid 10 nm Al_2O_3 gate dielectric with a self-assembled monolayer (SAM) made of 1-tetradecylphosphonic acid (TDPA) (thickness $d_{TDPA} = 1.74$ nm [17]) was used. The chemical modification of the oxide surface results in a passivation of the gate-oxide due to the high packing density of the formed SAM [18, 19]. The improved electrical characteristics with a reduction of traps at the oxide– organic semiconductor (OSC) interface, reduced leakage currents and the tunability of the threshold voltage (V_{th}) has been widely investigated [20–23]. In a second approach we used hexagonal boron nitride (hBN) with high breakdown voltages ranging from 0.8 [24] to 1.2 V nm^{-1} [25] as a dielectric. In the field of two-dimensional materials, using hBN both as a dielectric substrate or to completely encapsulate graphene is well established and has shown to drastically increase the electrical characteristics in terms of increased mobility and reduced charge disorder [26–29], which is mainly related to a reduction of surface charge traps. However, in the field of OSCs, there are only a few reports demonstrating the potential of hBN as a dielectric to facilitate improved charge transport properties yet [30–32]. In order to maintain the atomical flatness of hBN, graphite consisting of several graphene layers was used as gate electrode and contacted with an additional gold lead. After gate electrode fabrication and solution-based single PDPP fiber deposition, individual fibers were located via atomic force microscopy (AFM) (see figure 1(c) for Al_2O_3/TDPA and supplementary figure 1 for hBN) and finally precisely contacted via electron beam lithography. Further details can be found in the experimental section. Line traces in figure 1(d) of two different fibers reveal heights of 2 nm and 3 nm, respectively, which demonstrates that even the thinnest agglomerates that we can identify using AFM consist

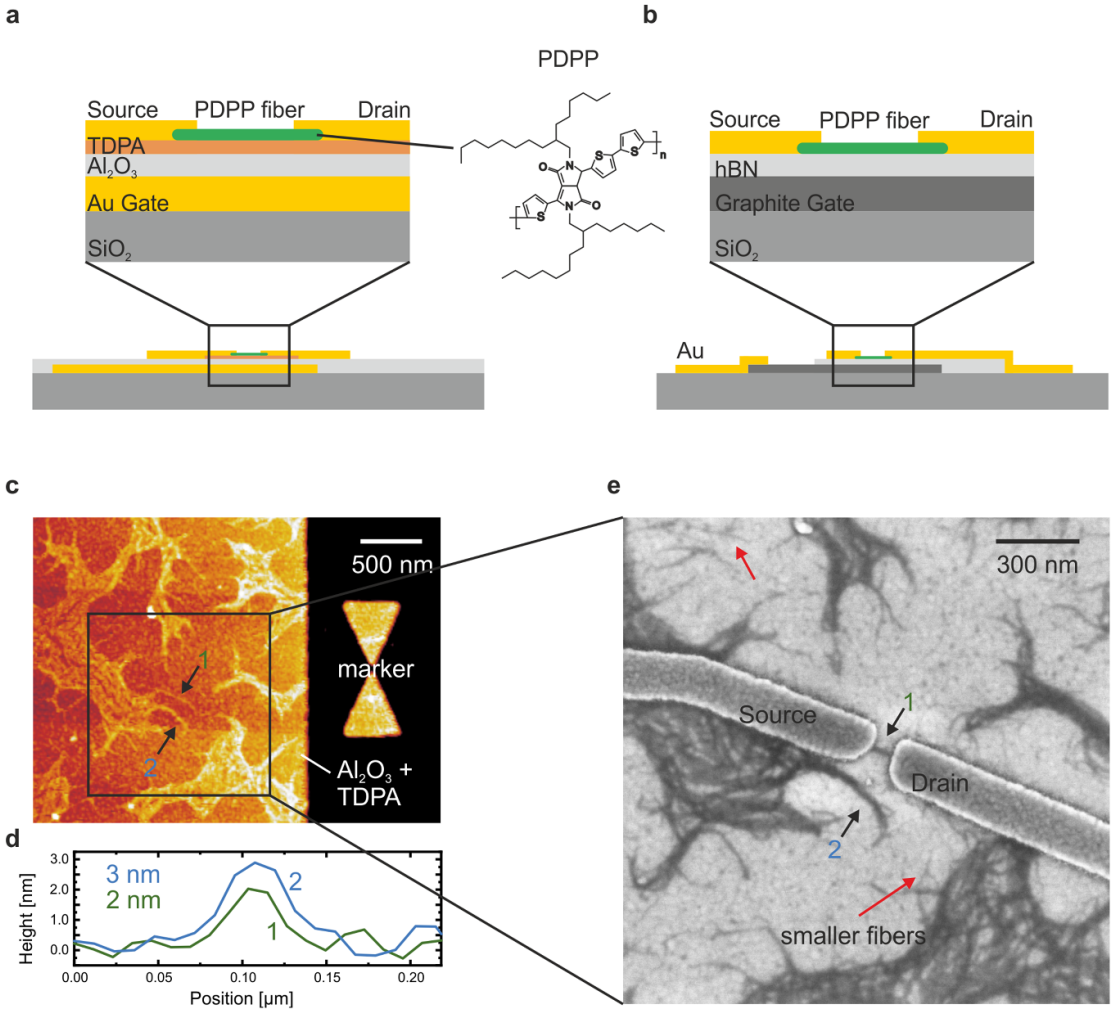

Figure 1. Single PDPP fiber transistor. Schematic illustration of the device geometry with (a) a hybrid Al_2O_3/TDPA gate dielectric and (b) an hBN dielectric with graphite electrode configuration. (c) AFM image of PDPP fibers deposited on Al_2O_3/TDPA. (d) Line traces across two different fibers reveal thicknesses of 2 nm and 3 nm. (e) SEM image of the same region of an electrically contacted fiber displays fibers that are not resolvable with AFM (indicated by red arrows).

of multiple polymer chains. This is confirmed in the scanning electron microscopy (SEM) image of an electrically contacted fiber in figure 1(e), in which also smaller fibers not resolvable via AFM become visible. Hence, the term 'single fiber' refers to individual fibers consisting of several well aligned parallel polymer chains, schematically illustrated in supplementary figure 2 and confirmed by [16]. Even though a comparison of the AFM image after fiber deposition and the SEM image after contact patterning indicates that PDPP is not affected by the electron beam lithography process (poly(methyl methacrylate) (PMMA) deposition, 120 °C soft bake, lift-off in acetone and isopropanol)
(see experimental section), small damage or conformational changes cannot be fully excluded.

Figure 2 shows the room-temperature electrical characteristics of single PDPP fiber transistors with either Al_2O_3/TDPA or hBN as a dielectric. In the case of Al_2O_3/TDPA (figures 2(a) and (b)), despite a channel length of only 56 nm, the output curves exhibit fully saturating currents indicating the good gate coupling. The increasing offset for $V_{DS} = 0$ V is related to an increasing gate-leakage current for higher V_{GS}. The saturation transfer characteristics reveal an on-off ratio of 6000 and a subthreshold swing of 250 mV dec^{-1} with a threshold voltage of $V_{th} = -0.89$ V. The weakly V_{GS} and hence carrier-density-dependent hole mobility (see supplementary figure 3(a)) of $\mu_{sat} \approx 0.3$ cm^2 V^{-1} s^{-1} (at $V_{GS} = -1$ to -1.5 V) for an assumed channel width of $W = 3$ nm (fiber diameter) is quite high given that wet processing of the fibers was used, but is a factor of 10 lower compared to macroscopic devices with channel lengths of 200 μm [33]. In the case of hBN as dielectric, the output curves exhibit saturating behavior for a channel length of 67 nm (figure 2(c)) and even start to saturate for channel lengths of only 25 nm (figure 2(e)). It has to be noted that the saturating behavior might also be influenced by a decreasing gate current I_G for increasing V_{DS} (especially for the device in figure 2(c)). While for the single fiber in figure 2(d), a mobility of $\mu_{sat} = 8 \times 10^{-3}$ cm^2 V^{-1} s^{-1} (at $V_{GS} = -4.75$ to -5.75 V) can be extracted, the mobility of the device in

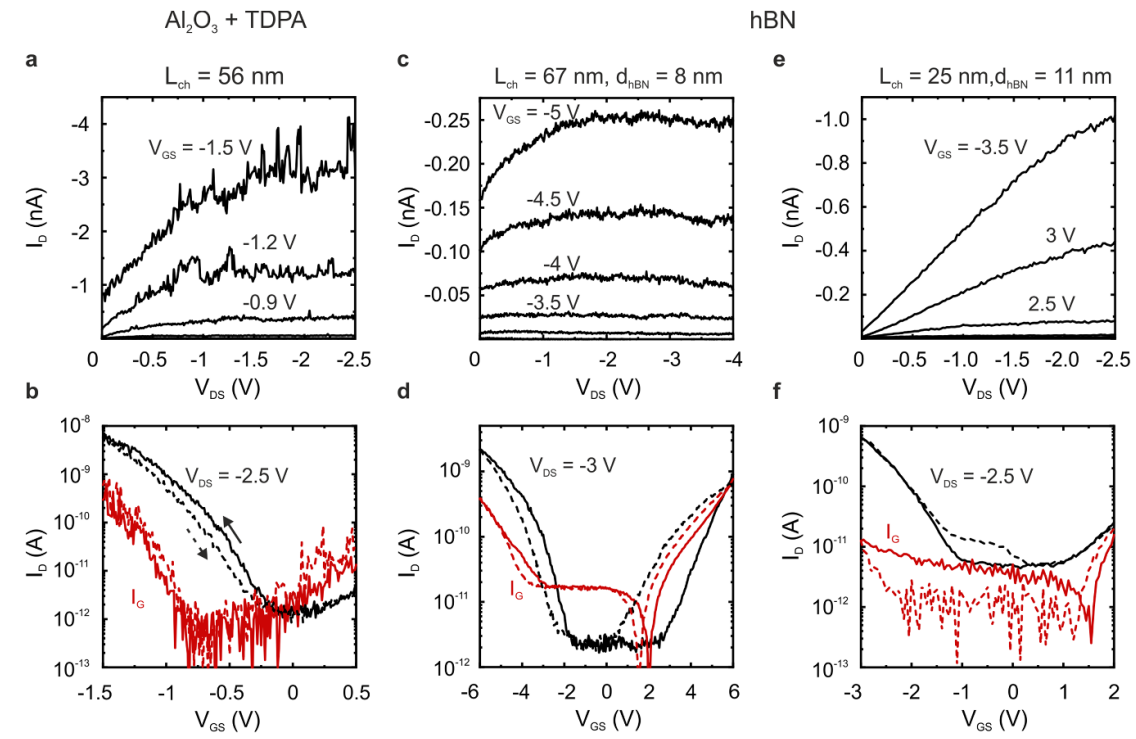

Figure 2. Electrical characteristics of single PDPP fiber transistors. (a) Output and (b) transfer characteristics in the saturation regime (black) with corresponding gate current I_G (red) on an Al_2O_3/TDPA hybrid gate dielectric (channel length $L_{ch} = 56$ nm, $T_{set} = 300$ K) (c), (d) electrical characteristics on hBN with a thickness of $d_{hBN} = 8$ nm ($L_{ch} = 67$ nm) and (e), (f) with a thickness of $d_{hBN} = 11$ nm ($L_{ch} = 25$ nm). The real sample temperature was lower due to poor thermal coupling (see experimental section for further explanation). The solid lines represent the forward and the dashed lines the backwards sweep direction.

figure 2(f) exhibits no V_{GS} independent region (see supplementary figure 3(a)). Additionally, when hBN is used as gate dielectric, ambipolar transport can be observed (see also figure 3).

While it is remarkable that using comparably crude e-beam patterning and solvent processing tools, nanoscale transistors consisting of individual polymer nanofibers can be fabricated, the charge carrier mobility in these transistors is smaller than in thin film transistors made from the same polymer [33]. While we fabricated the transistors with the hope to reach the intrachain transport regime (which should allow for significantly higher charge carrier mobility), the reason for the lower mobility is unclear. One potential reason could be contact resistance that would explain the comparably very large required V_{DS} values for transport. Another explanation could be that in macroscopic devices charge transport is an average effect of different efficient conduction paths where always paths of highest conductance can form, compared to single fiber transistors where transport is strongly restricted and by chance we have not contacted fibers with *a-priori* low energetic disorder and hence good charge transport.

To understand in more depth the charge transport processes in our devices, we have reverted to analyzing the temperature dependence of the mobility [5]. Figure 3 shows the electrical characteristics of a single PDPP fiber transistor on hBN for 300 K and 10 K. Interestingly, when using hBN as a gate dielectric, ambipolar charge transport could be observed even at cryogenic temperatures (see also supplementary figure 4 for another device). One of the major requirements that has to be ensured to realize ambipolar charge transport in organic field-effect transistors is a trap-free gate dielectric [34, 35]. The observation of ambipolar transport elucidates the high potential of using hBN as a gate dielectric also in the field of organic electronics. With decreasing temperature, the threshold voltage V_{th} in the transfer characteristics shifts to more negative values for $V_{GS} < 0$ and to more positive values for $V_{GS} > 0$, can be explained by the filling of shallow and deep trap states [36, 37]. While the mobility decreases significantly with decreasing temperature for smaller drain-source voltages V_{DS} (see supplementary figure 5), its temperature dependence is less pronounced for higher positive and negative V_{DS} (figures 3(c) and (d)). As the devices might suffer from large contact resistances it would be very helpful to be able to extract the contact resistance in a reliable manor. Since however our devices only work in the saturation regime, methods that have been used to extract contact resistances like e.g. the Y-function method [38] are not applicable. Consequently, four-point probe measurements or saturation transfer measurements that maintain the channel pinch-off at the drain contact

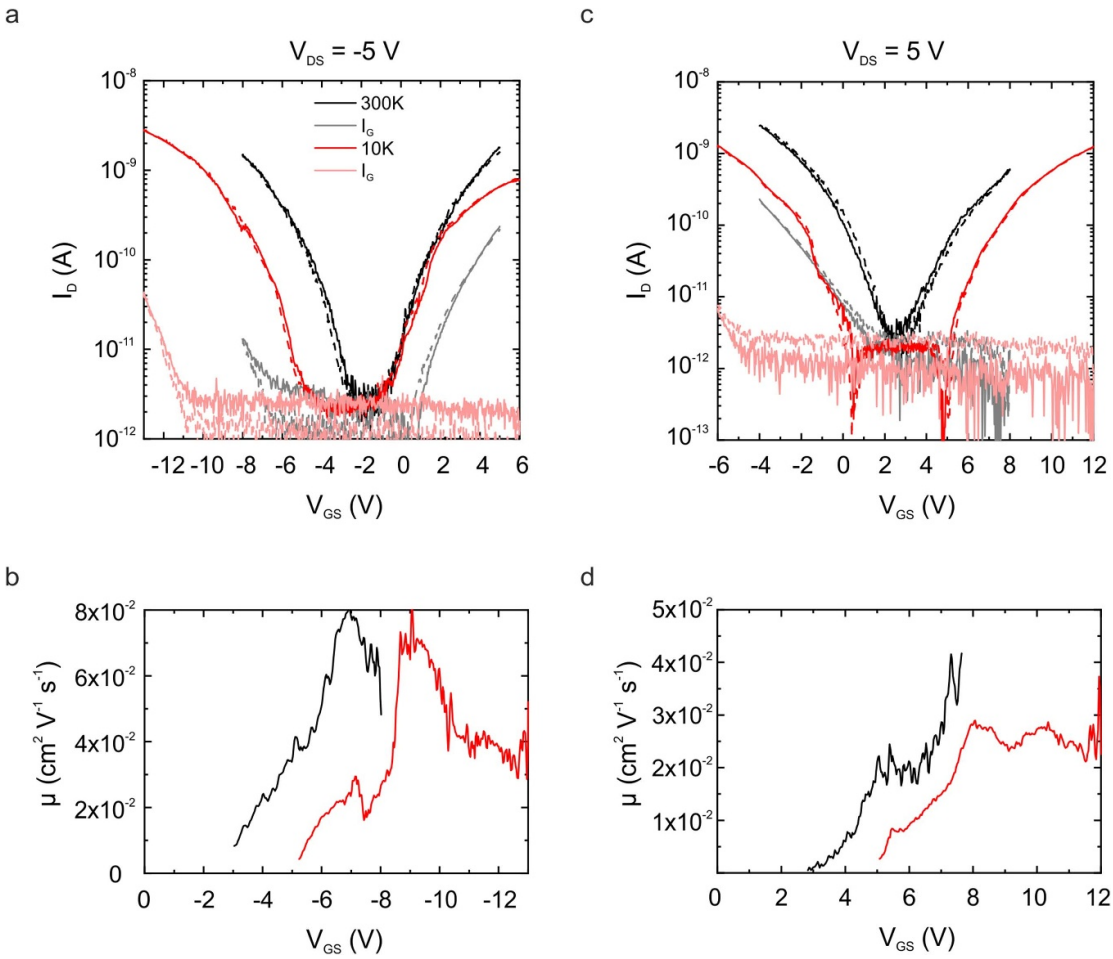

Figure 3. Transfer and mobility characteristics of a single PDPP fiber transistor on hBN ($d_{hBN} = 25$ nm) at $T_{set} = 300$ K (black) and $T_{set} = 10$ K (red). (a), (b) Electrical measurements for $V_{DS} = -5$ V and (c), (d) electrical measurements for $V_{DS} = 5$ V. The solid lines represent the forward and the dashed lines the backwards sweep direction. The corresponding gate current I_G is shown in grey for $T_{set} = 300$ K and bright red for $T_{set} = 10$ K. The mobility is only shown for $|V_{on}| \leq |V_{GS}|$, where $|I_D| \geqslant |I_G|$.

($V_{DS} = V_{GS} - V_{th}$) would be necessary to further elaborate on the temperature dependent mobility behavior [39].

Here it should be emphasized that the presented results are not a macroscopic average measure. In fact, due to the individuality of each device, where e.g. small deviations in the fiber composition, different channel lengths, variations in gate coupling or contact effects strongly influence the electrical characteristics, each device has to be treated separately. Apart from the above weakly temperature dependent mobility from $T = 300$ K to $T = 10$ K at high V_{DS}, some devices also exhibited strongly thermally activated transport with a transport freeze-out at lower temperatures (see supplementary figure S6). Interestingly, for some devices the transport starts to deviate from the behavior at elevated temperatures by the formation of plateaus in the first place when cooling down, as indicated in supplementary figure 5(a) for 10 K. If the system is cooled down further, the transport in these quasi 1D-systems starts to oscillate, which is indicative of Coulomb physics.

The evolution of these Coulomb oscillations can be seen in supplementary figure 7. The I–V curves of another device at base temperature ($T = 5.5$ K) in figure 4(a) exhibit several irregularly spaced current peaks with varying amplitudes, highlighted with black arrows. Furthermore, it can clearly be seen that the gate current noise (red curve) has no influence on the measured oscillations. Figures 4(b) and (c) show the corresponding current and differential conductance $\partial I_D/\partial V_{GS}$ maps as a function of V_{GS} and V_{DS}. The current is blocked in the dark blue region in a range of $|V_{DS}| \lessapprox 0.6$ V. At small V_{DS} and sufficiently small temperatures, the energy needed to add an extra charge carrier to an at least in one direction restricted system (single fibers in our case), can be larger than the thermal energy. In this case, the number of charge carriers in the system is fixed and charge transport through the system is blocked, which refers to Coulomb blockade. Upon varying V_{GS} and V_{DS}, the chemical potential inside the system respectively of the drain electrode can be tuned, resulting in state configurations, where charge carries can tunnel through the system. Hence, the number of charge carriers can fluctuate and transport is allowed. Each of these resonances at specific V_{GS}

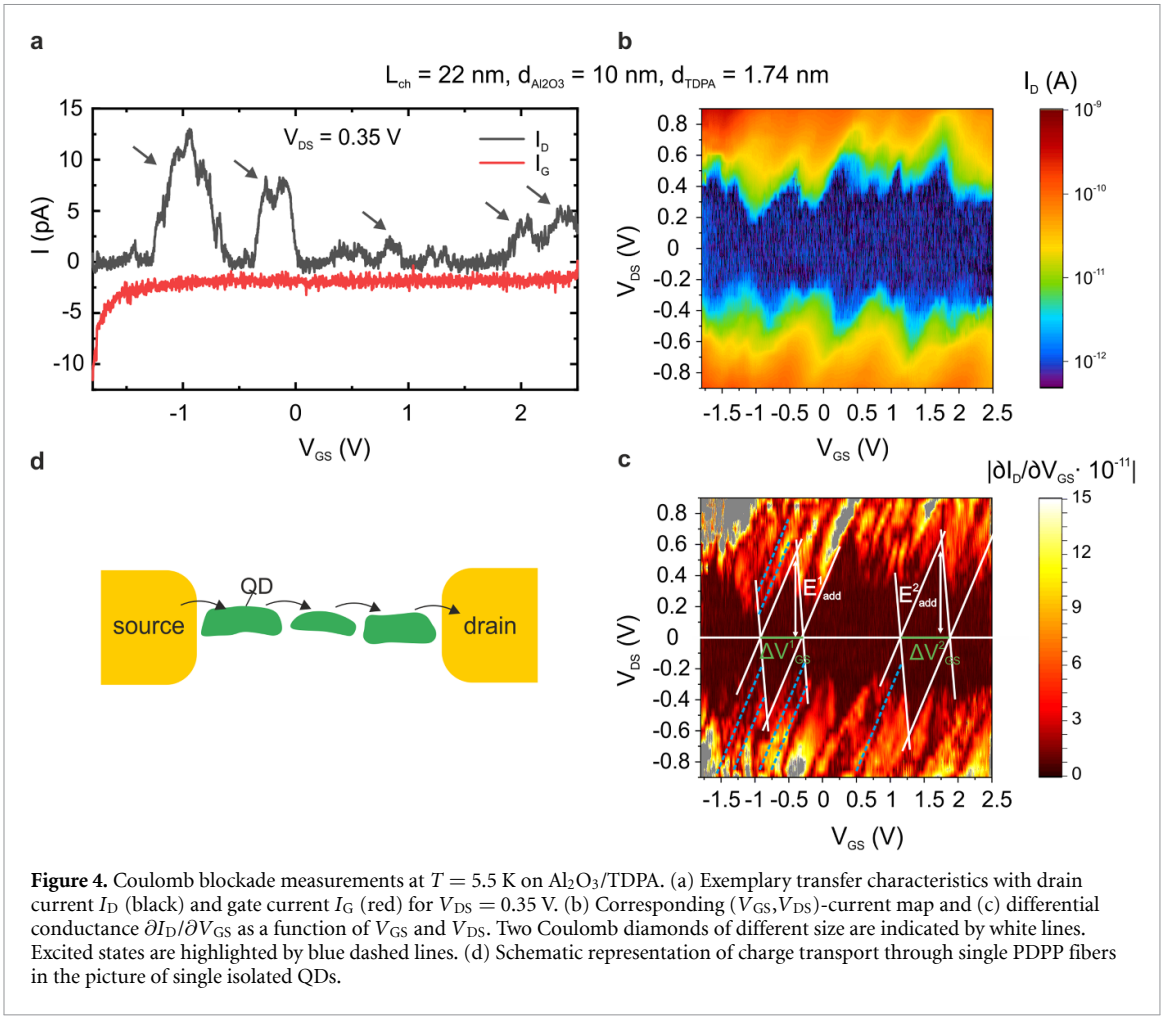

Figure 4. Coulomb blockade measurements at $T = 5.5$ K on Al_2O_3/TDPA. (a) Exemplary transfer characteristics with drain current I_D (black) and gate current I_G (red) for $V_{DS} = 0.35$ V. (b) Corresponding (V_{GS},V_{DS})-current map and (c) differential conductance $\partial I_D/\partial V_{GS}$ as a function of V_{GS} and V_{DS}. Two Coulomb diamonds of different size are indicated by white lines. Excited states are highlighted by blue dashed lines. (d) Schematic representation of charge transport through single PDPP fibers in the picture of single isolated QDs.

and V_{DS} values causes two straight lines in the $\partial I_D/\partial V_{GS}$ maps separating regions where current is blocked and allowed, resulting in typical Coulomb diamonds. Although indications of Coulomb blockade physics has been identified in polymer nanofibers [40, 41] and OSC thin film devices [42, 43], Coulomb diamonds have only been presented for single molecule [44–46] devices in the field of organic materials. Here we present the first observation of Coulomb diamonds for larger than single molecule organic devices. The clearly visible Coulomb diamonds are irregular and exhibit different sizes and shapes, which results from a superposition of different sized Coulomb diamonds with addition energies ranging from $E_{add} = 0.56$ eV to 0.63 eV.

In the $\partial I_D/\partial V_{GS}$ map, various excited states are visible as lines running parallel to the Coulomb diamond edge, some of them highlighted by blue dashed lines. In general, aside from addition energies, stability diagrams can also be used for spectroscopic investigations to explore excited states which emerge additionally to the ground state configuration [47]. These excited states can be electronic or vibrational in nature. *A priori* we can only speculate about the origin of the observed excited states here. Although they do not appear very sharp, excitation energies varying from $E_{ex} = 0.17$ eV to 0.28 eV can be estimated. For similar polymers Barszcz *et al* [48] identified the C–C stretching vibration of thiophene rings at ≈0.173 eV and the in-phase C=C stretching of the DPP core at ≈0.2 eV. Similar results have been presented by Adil *et al* [49], Francis *et al* [50] and Dorfner *et al* [51]. If we assume coupling to the phonon modes as the origin for the excited states, these results compare very well with the electrically measured results in this work, which proves that excited states can be investigated also for OSCs via charge transport measurements. To do so, further device optimization as e.g. further reducing the channel length or contacting thinner fibers, would be necessary in order to get sharper diamond edges as well as lines induced by excited states. It has to be noted that the excited states are only visible on one side of the Coulomb diamond for positive slopes which is related to asymmetric coupling and hence different tunnel barriers for the source and drain electrode [47, 52]. The asymmetric coupling is also evident from the sheared diamonds. The different tunnel barriers are evident from supplementary figure 8. Upon exchanging the source and drain electrodes in two consecutive measurements, the size, shape and position of the Coulomb oscillations change.

In all measurements the Coulomb diamonds are not closed near $V_{DS} = 0$ V (see supplementary figure 9 for another example). The occurring gap in addition with different sizes and shapes of the diamonds has been widely investigated [53–58] and is caused by an array of single quantum dots (QDs) with multiple tunnel junctions, schematically illustrated in figure 4(d) [40]. Within a single fiber, composed of several PDPP polymer chains, when cooling down several different conduction paths between different chains with energetic disorder-broadened polaronic states are available. In a schematic representation, one path of highest conductance is formed between several QDs. These different QDs with different capacitances are connected via tunnel barriers. Transport is then dominated by the junction with the largest barrier within this path of highest conductance. Since individual diamonds are distinguishable in the $\partial I_D/\partial V_{GS}$ maps, the number of conduction paths as well as the number of QDs in the channel is very small. The size of the smallest QDs, which dominates the electrical characteristics, can be estimated by comparing the backgate capacitance C_{bg} and the geometrical capacitance C_{geom} for nanowires (see supplementary information for a detailed description). For the device in figure 4(d), this leads to a QD length of $L_{Al2O3/TDPA} = 7.3$ nm. Considering a small number of QDs in the channel, this value is in good agreement with a channel length of 27 nm. For hBN as dielectric (see supplementary figure 10) the current is blocked in a range of $|V_{DS}| \lessapprox 1$ V in the dark blue region. However, the Coulomb diamonds are less regular and hence only partially visible in the $\partial I_D/\partial V_{GS}$ map. The addition energies varying from $E_{add} = 1.1$ eV to 1.8 eV as well as the gate voltage period of the Coulomb oscillations ΔV_G are increased compared to the devices with Al_2O_3/TDPA as a dielectric. These observations coincide with the estimated QD size of $L_{hBN} = 1.4$ nm for a channel length of 24 nm. One possible explanation could be that the different surface energies of hBN and TDPA (defined by different contact angles of 115° for TDPA [59] and 135° [60] for hBN) might lead to different fiber compositions with different sized quantum dots. Further potential reasons for the formation of larger QDs in the PDPP fibers on the hybrid Al_2O_3/TDPA dielectric could be related to reduced energetic disorder [61], potentially reduced dipolar disorder [62] due to the lower dielectric constant of TDPA compared to hBN [26, 63], or a different degree of crystallinity, within the transport path of highest conductance [7, 8]. This explanation is in agreement with the substantially higher mobilities observed in the PDPP fibers on the hybrid dielectric. To disentangle the influence of energetic disorder and different degrees of crystallinity on charge transport and hence QD sizes, further structural, spectroscopic and electrical transport measurements are required. With such additional measurements a direct correlation between QD sizes and the polaron coherence lengths could be established [3].

The transfer characteristics at room temperatures in figures 2 and 3 exhibit a clear off-state in the region around $V_{GS} = 0$ V, which is related to the band gap of $E_{gap} \approx 1.8$ eV of PDPP. Usually one would expect a zero-current region in the current maps with $N = 0$ charge carriers in the QD, reflecting the semiconducting gap corresponding to the off-current V_{GS} region of the transfer curves. This has been successfully demonstrated for carbon nanotube QDs [64, 65]. The tendency of a full depletion with an emptied QD can be seen to some extent in supplementary figure S11. In all other devices however this behavior was not observable. One possible explanation could be that at elevated temperatures, charge transport is dominated by thermally excited charge carriers. When cooling down, more and more charges are trapped in localized states resulting in reduced currents (see supplementary figure S7 $T = 300$ K to T = 100 K). One possible explanation for the occurring oscillations in the off-current region for high temperatures could be that instead of the classical Coulomb blockade regime, our devices operate in the quantum Coulomb blockade regime [66]. Here, once entering the quantum regime, the intensity of Coulomb oscillations increases with decreasing temperature. In other words, Coulomb oscillations might become visible in the off-region only when cooling down the system. Presumably for most devices, a complete emptied fiber cannot be achieved due to the priorly dielectric breakdown when increasing V_{GS}. In order to investigate this in more detail and especially to differentiate between the classical and the quantum Coulomb blockade regime, however, further measurements would be beneficial.

3. Conclusion

In conclusion, we fabricated single polymer fiber transistors with channel lengths below 100 nm and investigated charge transport dynamics from room to cryogenic temperatures. Utilizing ultrathin Al_2O_3/TDPA respectively hBN gate dielectrics resulted in almost ideal electrical characteristics despite such short channel lengths. Although the devices suffer from large contact resistances resulting in reduced mobilities compared to macroscopic devices, temperature dependent measurements indicate a weakly temperature-dependent mobility for large V_{DS} from $T = 300$ K to $T = 10$ K. For some devices at very low temperatures, the transport in these quasi-1D systems can be attributed to Coulomb blockade effects due to the observation of Coulomb oscillations and Coulomb diamonds. It was shown that the fiber consists of an array of multiple QDs which are separated by tunnel barriers. In addition, we demonstrated that by further

device optimization excited states could be investigated by charge transport measurements. Our measurements show that nanoscale contacting can be a viable tool to address charge transport at the nanoscale in semiconducting polymers relevant in organic photovoltaics and field-effect transistors.

4. Experimental section

To avoid degradation of the PDPP polymer all fabrication steps involving exposure to ambient conditions were performed in an ozone cleaned atmosphere.

4.1. Electrode fabrication

All structures were patterned by electron beam lithography (e-line system, Raith) using the following parameters: 10 kV, 108 μC cm^{-2} for 10 μm, 145 μC cm^{-2} for 30 μm and 165 μC cm^{-2} for 60 μm aperture. A 4.5 wt.% solution of the positive-resist PMMA 950 k dissolved in anisole (AR-P 672.045, Allresist) was spin coated at 800 rpm for 1 s and 4000 rpm for 30 s followed by a 3 min 150 °C bake (5 min at 120 °C for top contacts to prevent thermal damage of PDPP). The exposed structures were developed in a 1:3 solution of methylisobutylketon:isopropanol for 1 min 45 s. For structures smaller than 100 nm, a high-contrast developer with the addition of 2% methylethylketone was used [67]. The gate electrodes were formed via electron-beam physical vapor deposition of 1 nm Cr (@ 0.3 Å s^{-1}) and 30 nm Au (@ 1 Å s^{-1}) at pressures $<5 \times 10^{-7}$ mbar. Top contacts on PDPP were fabricated through thermal evaporation of 0.3 nm titanium (at 0.1 Å s^{-1}) and 30 nm gold (at 1 Å s^{-1}) at a pressure of $\sim 5 \times 10^{-6}$ mbar.

4.2. Al_2O_3/TDPA gate

After patterning the local Au gate contacts, 10 nm of Al_2O_3 was deposited on the whole substrate via radiofrequency (RF) sputtering (40 W, Ar pressure of 2×10^{-2} mbar). In a next step, the TDPA SAM was locally deposited (areas patterned by electron beam lithography) on the prefabricated gate electrodes by initially applying a 1 min oxygen plasma (ICP-RIE, Plasmalab System 100, Oxford Instruments, RF power of 200 W, IPC power of 70 W, a O_2 flow of 30 sccm and a pressure of 10 mTorr) followed by immediately immersing the sample in a 1 mM solution of TDPA in isopropanol for 2 h. Finally, the substrates were baked for 5 min at 150 °C.

4.3. hBN gate with graphite electrode

Few-layer hBN and graphene were fabricated on pre-cleaned and hydrofluoric acid etched substrates by mechanical exfoliation from the bulk material. The detailed procedure for few-layer hBN as well as a description of the stamp fabrication can be found in the methods section of our previous work [15]. Graphene exfoliation is completely analogous with the only difference of using directly the as-received natural graphite bulk instead of crushed small crystals. In order to fabricate hBN gates with graphite electrodes a stamping method was adopted from [68, 69]. A detailed description can be found in the supplementary information. The graphite gate contact is contacted with gold in an additional electron beam lithography step.

4.4. Single PDPP fiber deposition

Single PDPP fibers on a local Al_2O_3/TDPA gate were deposited by immersing the sample overnight in a 0.02 wt.% solution of PDPP in 1,3-meta-dichlorobenzene at room temperature. The solution was previously stirred at least for 6 h at 80 °C. The sample was blow-dried with nitrogen and baked for 5 min at 80 °C.

Single PDPP fibers on hBN were deposited in two different ways. One approach is completely analogous as above with the exception that a 0.2 wt.% solution was used. In another approach a 0.05 wt.% solution was drop casted on the substrate. Subsequently the droplet was slowly blown over the hBN-graphite stack with nitrogen, resulting in a very thin remaining layer of the PDPP solution. The sample was dried at room temperature and subsequently baked for 5 min at 80 °C.

4.5. Electrical characterization

Measurements were performed in a Lakeshore CRX-VF probe station under vacuum (temperature range 5 K–450 K). Electrical contacting is realized via needle probes. In order to ensure sufficient thermal anchoring the substrates were glued with silver-conducting paint on the substrate holder of the probe station. However, some devices were only placed on the cooled chuck without silver-conducting paint. Here, at elevated temperatures, the real temperature of the sample is smaller than the setpoint temperature T_{set} due to the contacted probes with a temperature of 10 K−15 K and a bad thermal contact of the sample to the chuck, resulting in a temperature offset of up to 50 K for a setpoint temperature of $T_{set} = 300$ K. While quantitative data evaluation is not possible in these cases, qualitative statements are still valid. The gate

voltage V_{GS} was applied with a Keithley 2450 and the gate current I_G simultaneously measured. The drain voltage V_{DS} was applied with a Yokogawa 7651 DC source. To allow highly accurate current measurements down to the sub-nA regime the drain current I_D was measured with a current preamplifier (1211 DL Instruments) and a HP 34401 A voltmeter.

Data availability statement

The data that support the findings of this study are available upon request from the authors.

Acknowledgments

J L and R T W acknowledge funding from the Center for Nanoscience (CeNS) and the SolarTechnologies go Hybrid (SolTech) initiative. We additionally acknowledge funding by the Deutsche Forschungsgemeinschaft (DFG, German Research Foundation) under Germany's Excellence Strategy 'EXC 2089 /1—390776260 (e-conversion)'. K W and T T acknowledge support from JSPS KAKENHI (Grant Nos. 19H05790 and 20H00354).

Author contribution

The experiments were conceived and designed by J L and R T W, J L prepared the samples, conducted the measurements and data analysis. All authors discussed the results. M S helped with the data analysis. J L, M S and R T W wrote the manuscript with the input of all authors. R T W supervised the project. K W and T T synthesized the hBN crystals.

ORCID iDs

Martin Statz https://orcid.org/0000-0001-7791-3981
K Watanabe https://orcid.org/0000-0003-3701-8119
Frank Ortmann https://orcid.org/0000-0002-5884-5749
R Thomas Weitz https://orcid.org/0000-0001-5404-7355

References

[1] Noriega R, Rivnay J, Vandewal K, Koch F P V, Stingelin N, Smith P, Toney M F and Salleo A 2013 *Nat. Mater.* **12** 1038
[2] Gu K, Snyder C R, Onorato J, Luscombe C K, Bosse A W and Loo Y-L 2018 *ACS Macro Lett.* **7** 1333
[3] Chew A R, Ghosh R, Pakhnyuk V, Onorato J, Davidson E C, Segalman R A, Luscombe C K, Spano F C and Salleo A 2018 *Adv. Funct. Mater.* **28** 1804142
[4] Keene S T *et al* 2022 *J. Am. Chem. Soc.* **144** 10368
[5] Lenz J and Weitz R T 2021 *APL Mater.* **9** 110902
[6] Chang J-F, Sirringhaus H, Giles M, Heeney M and McCulloch I 2007 *Phys. Rev.* B **76** 205204
[7] Di Pietro R *et al* 2016 *Adv. Funct. Mater.* **26** 8011
[8] Statz M, Venkateshvaran D, Jiao X, Schott S, McNeill C R, Emin D, Sirringhaus H and Di Pietro R 2018 *Commun. Phys.* **1** 16
[9] Borchert J W, Weitz R T, Ludwigs S and Klauk H 2022 *Adv. Mater.* **34** e2104075
[10] Wang J, Zhang F, Zhang M, Wang W, An Q, Li L, Sun Q, Tang W and Zhang J 2015 *Phys. Chem. Chem. Phys.* **17** 9835
[11] Nielsen C B, Turbiez M and McCulloch I 2013 *Adv. Mater.* **25** 1859
[12] Yi Z, Wang S and Liu Y 2015 *Adv. Mater.* **27** 3589
[13] Kettner M, Zhou M, Brill J, Blom P W M and Weitz R T 2018 *ACS Appl. Mater. Interfaces* **10** 35449
[14] Lenz J, Del Giudice F, Geisenhof F R, Winterer F and Weitz R T 2019 *Nat. Nanotechnol.* **14** 579
[15] Lenz J, Seiler A M, Geisenhof F R, Winterer F, Watanabe K, Taniguchi T and Weitz R T 2021 *Nano Lett.* **21** 4430
[16] Pandey M, Kumari N, Nagamatsu S and Pandey S S 2019 *J. Mater. Chem.* C **7** 13323
[17] Lee J, Kim J H and Im S 2003 *Appl. Phys. Lett.* **83** 2689
[18] Weitz R T, Zschieschang U, Forment-Aliaga A, Kälblein D, Burghard M, Kern K and Klauk H 2009 *Nano Lett.* **9** 1335
[19] Weitz R T, Zschieschang U, Effenberger F, Klauk H, Burghard M and Kern K 2007 *Nano Lett.* **7** 22
[20] Aghamohammadi M, Rödel R, Zschieschang U, Ocal C, Boschker H, Weitz R T, Barrena E and Klauk H 2015 *ACS Appl. Mater. Interfaces* **7** 22775
[21] Chua L-L, Zaumseil J, Chang J-F, Ou E C-W, Ho P K-H, Sirringhaus H and Friend R H 2005 *Nature* **434** 194
[22] Kelley T W, Boardman L D, Dunbar T D, Muyres D V, Pellerite M J and Smith T P 2003 *J. Phys. Chem.* B **107** 5877
[23] Sekitani T, Zschieschang U, Klauk H and Someya T 2010 *Nat. Mater.* **9** 1015
[24] Lee G-H, Yu Y-J, Lee C, Dean C, Shepard K L, Kim P and Hone J 2011 *Appl. Phys. Lett.* **99** 243114
[25] Hattori Y, Taniguchi T, Watanabe K and Nagashio K 2015 *ACS Nano* **9** 916
[26] Dean C R *et al* 2010 *Nat. Nanotechnol.* **5** 722
[27] Wang L *et al* 2013 *Science* **342** 614
[28] Yankowitz M, Ma Q, Jarillo-Herrero P and LeRoy B J 2019 *Nat. Rev. Phys.* **1** 112
[29] Weitz R T and Yacoby A 2010 *Nat. Nanotechnol.* **5** 699
[30] Kang S J, Lee G-H, Yu Y-J, Zhao Y, Kim B, Watanabe K, Taniguchi T, Hone J, Kim P and Nuckolls C 2014 *Adv. Funct. Mater.* **24** 5157
[31] Zhang Y *et al* 2016 *Phys. Rev. Lett.* **116** 16602

[32] Renn L, Walter L S, Watanabe K, Taniguchi T and Weitz R T 2022 *Adv. Mater. Interfaces* **9** 2101701
[33] Kettner M, Mi Z, Kälblein D, Brill J, Blom P W M and Weitz R T 2019 *Adv. Electron. Mater.* **5** 1900295
[34] Zaumseil J and Sirringhaus H 2007 *Chem. Rev.* **107** 1296
[35] Risteska A and Knipp D (eds) 2016 *Organic Ambipolar Transistors and Circuits. Handbook of Visual Display Technology* (Cham: Springer) (https://doi.org/10.1007/978-3-319-14346-0_177)
[36] Terao S, Hirai T, Morita N, Maeda H, Kojima K and Tachibana M 2010 *J. Appl. Phys.* **108** 124511
[37] Sakanoue T and Sirringhaus H 2010 *Nat. Mater.* **9** 736
[38] Xu Y, Minari T, Tsukagoshi K, Chroboczek J A and Ghibaudo G 2010 *J. Appl. Phys.* **107** 114507
[39] Di Pietro R, Venkateshvaran D, Klug A, List-Kratochvil E J W, Facchetti A, Sirringhaus H and Neher D 2014 *Appl. Phys. Lett.* **104** 193501
[40] Aleshin A N, Lee H J, Jhang S H, Kim H S, Akagi K and Park Y W 2005 *Phys. Rev.* B **72**
[41] Akai-Kasaya M, Ogawa N and Kakinoki S 2020 *IOP Conf. Ser.: Mater. Sci. Eng.* **835** 12017
[42] Schoonveld W, Fichou D, Bobbert B, van Wees J and Klapwijk T M 2000 *Nature* **404** 977
[43] Akai-Kasaya M, Okuaki Y, Nagano S, Mitani T and Kuwahara Y 2015 *Phys. Rev. Lett.* **115** 196801
[44] Selzer Y and Allara D L 2006 *Annu. Rev. Phys. Chem.* **57** 593
[45] Kubatkin S, Danilov A, Hjort M, Cornil J, Brédas J-L, Stuhr-Hansen N, Hedegård P and Bjørnholm T 2003 *Nature* **425** 698
[46] Osorio E A, Bjørnholm T, Lehn J-M, Ruben M and van der Zant H S J 2008 *J. Phys.: Condens. Matter* **20** 374121
[47] Thijssen J M and van der Zant H S J 2008 *Phys. Status Solidi* b **245** 1455
[48] Barszcz B, Kędzierski K, Jeong H Y and Kim T-D 2017 *J. Lumin.* **185** 219
[49] Adil D, Kanimozhi C, Ukah N, Paudel K, Patil S and Guha S 2011 *ACS Appl. Mater. Interfaces* **3** 1463
[50] Francis C, Fazzi D, Grimm S B, Paulus F, Beck S, Hillebrandt S, Pucci A and Zaumseil J 2017 *J. Mater. Chem.* C **5** 6176
[51] Dorfner M F X, Hutsch S, Borrelli R, Gelin M F and Ortmann F 2022 *J. Phys. Mater.* **5** 24001
[52] Park H, Park J, Lim A K L, Anderson E H, Alivisatos A P and McEuen P L 2000 *Nature* **407** 57
[53] Danilov A V, Golubev D S and Kubatkin S E 2002 *Phys. Rev.* B **65**
[54] Babi B, Iqbal M and Schoenenberger C 2003 *Nanotechnology* **14** 327
[55] Mol J A, Lau C S, Lewis W J M, Sadeghi H, Roche C, Cnossen A, Warner J H, Lambert C J, Anderson H L and Briggs G A D 2015 *Nanoscale* **7** 13181
[56] Moriyama S, Morita Y, Yoshihira M, Kura H, Ogawa T and Maki H 2019 *J. Appl. Phys.* **126** 44303
[57] Nuryadi R, Ikeda H, Ishikawa Y and Tabe M 2003 *IEEE Trans. Nanotechnol.* **2** 231
[58] Otsuka T, Abe T, Kitada T, Ito N, Tanaka T and Nakahara K 2020 *Sci. Rep.* **10** 15421
[59] Qu J, Nie D, Liu C, Wang H and Chen G 2013 *Surf. Interface Anal.* **45** 1363
[60] Nayak A P, Dolocan A, LEE J, CHANG H-Y, Pandhi T, Holt M, Tao L I and Akinwande D 2014 *Nano* **09** 1450002
[61] Veres J, Ogier S D, Leeming S W, Cupertino D C and Mohialdin Khaffaf S 2003 *Adv. Funct. Mater.* **13** 199
[62] Shin N, Schellhammer K S, Lee M H, Zessin J, Hambsch M, Salleo A, Ortmann F and Mannsfeld S C B 2021 *Adv. Mater. Interfaces* **8** 2100320
[63] Fukuda K, Hamamoto T, Yokota T, Sekitani T, Zschieschang U, Klauk H and Someya T 2009 *Appl. Phys. Lett.* **95** 203301
[64] Aspitarte L, McCulley D R, Bertoni A, Island J O, Ostermann M, Rontani M, Steele G A and Minot E D 2017 *Sci. Rep.* **7** 8828
[65] Jarillo-Herrero P, Sapmaz S, Dekker C, Kouwenhoven L P and van der Zant H S J 2004 *Nature* **429** 389
[66] Kouwenhoven L P, Marcus C M, McEuen P L, Tarucha S, Westervelt R M and Wingreen N S 1997 *Mesoscopic Electron Transport* ed L L Sohn, L P Kouwenhoven and G Schön (Dordrecht: Springer) p 105
[67] Bernstein G H, Hill D A and Liu W-P 1992 *J. Appl. Phys.* **71** 4066
[68] Purdie D G, Pugno N M, Taniguchi T, Watanabe K, Ferrari A C and Lombardo A 2018 *Nat. Commun.* **9** 5387
[69] Zomer P J, Guimarães M H D, Brant J C, Tombros N and van Wees B J 2014 *Appl. Phys. Lett.* **105** 13101